Research Article

Abdul Aabid*, Muneer Baig and Meftah Hrairi

Ideal strain gauge location for evaluating stress intensity factor in edge-cracked aluminum plates

https://doi.org/10.1515/jmbm-2025-0083
received March 14, 2025; accepted September 19, 2025

Abstract: The stress intensity factor (SIF) must be determined accurately to analyze crack propagation and structural integrity in cracked material structures. This research focuses on improving the strain gauge location for single-ended fractured aluminum plates using a finite element method. The study examines the impact of fracture length-to-width ratios (a/W) on the estimation of r_{max}, the maximum allowed radial distance for accurate strain measurements. Strain fields under various mesh refinements were simulated using PLANE183 element from ANSYS software, and the results showed a strong association between mesh density. The results demonstrate that an improved strain gauge location greatly increases SIF measurement precision, limiting errors due to plasticity effects and strain gradients near the crack tip. Furthermore, mesh convergence studies show that mesh refinement produces negligible gains after a crucial refinement level. This study offers helpful recommendations for the positioning of strain gauges in fractured mechanics applications, guaranteeing precise SIF assessment for failure avoidance. Finally, confirmation against previous research shows a relative error of less than 3%, confirming the suggested methodology's dependability.

Keywords: stress intensity factor, strain gauge optimization, edge-cracked plate, mesh convergence, finite element modeling

Nomenclature

a	crack length
A_m, B_m	coefficients of series-type complex analytic functions for Mode I
C_m, D_m	coefficients of series-type complex analytic functions for Mode II
E	Young's modulus
G	Shear modulus
H	half height of the plate
K_1	Mode I stress intensity factor
r	radial distance from the crack-tip
r_{max}	upper limit for gauge locations along the gauge line
R^2	coefficient of determination
ν	Poisson's ratio
W	width of the plate
x, y – x, and y	coordinates of a point
Z	complex variable
Z_I, Y_I	complex analytic functions for Mode I
α	orientation angle of the strain gauge
θ	angular coordinate
φ_I	Airy stress function for Mode I
σ_x	normal stress in x direction
σ_y	normal stress in y direction
τ_{xy}	shear stress in x–y plane
ε_x	normal strain in x direction
ε_y	normal strain in y direction
γ_{xy}	shear strain in x–y plane
ε_x'	normal strain in x' direction
ε_{α^+}	normal strain in positive α direction
ε_{α^-}	normal strain in the negative α direction

Abbreviations

2D	two-dimensional
3D	three-dimensional
DIC	digital image correlation
DS technique	Dally and Sanford single-strain gauge technique

*** Corresponding author: Abdul Aabid,** Department of Engineering Management, College of Engineering, Prince Sultan University, PO BOX 66833, Riyadh, 11586, Saudi Arabia, e-mail: aaabid@psu.edu.sa
Muneer Baig: Department of Engineering Management, College of Engineering, Prince Sultan University, PO BOX 66833, Riyadh, 11586, Saudi Arabia
Meftah Hrairi: Department of Mechanical Engineering, Faculty of Engineering, International Islamic University Malaysia, P.O. Box 10, Kuala Lumpur, 50725, Malaysia

FE	finite element
NE	number of elements
NN	number of nodes
SIF	stress intensity factor

1 Introduction

Both theoretical and experimental approaches can be used to identify the parameters of the damaged structure in fracture mechanics. In particular, strain gauge methods or digital image correlation (DIC) can be used to assess the stress intensity factor (SIF) for a damaged aluminum plate under plane stress circumstances [1]. Strain gauge approaches have been proven to be an efficient and useful way to measure strain close to the crack zone, even though DIC needs high-resolution infrared cameras, which makes it an expensive option for strain measurement. The SIF for the damaged structure is then calculated using these strain data. Numerical and experimental methods, such as finite element (FE) analysis, offer important insights into fracture mechanics. To allow for precise SIF determination, the experimental method places strain gauges in key locations close to the crack zone. Research, such as that conducted by Sarangi *et al.* [2], has shown that the accuracy of the measured SIF is greatly impacted by the radial position of strain gauges. Errors may be introduced by plasticity and three-dimensional effects if the strain gauges are positioned too near the crack tip. On the other hand, positioning them too far away from the fractured tip might make it impossible to precisely capture the singularity-dominated strain field. To ensure accurate experimental results, Sarangi *et al.* suggested a system for determining the maximum allowable radial location (r_{max}) for appropriate strain gauge placement.

The main goal of this study is to use the FE analysis to identify the best place for strain gauges close to the crack zone in a thin aluminum plate. By examining the strain field, the FE technique simulates crack progression and establishes the ideal gauge locations. Additionally, this study confirms the current findings with available experimental data, guaranteeing the validity of the suggested methodology in calculating SIF for aluminum structures that have been damaged.

2 Related work

Over several decades, the study of strain gauge techniques and SIFs has evolved. A straightforward experimental method for determining Mode I SIF in orthotropic composites using strain gauges was proposed by Shukla *et al.* [3] in 1989. To increase accuracy, they determined the best location for the strain gauge and created theoretical equations for the strain field close to the crack tip. Glass-epoxy samples were used to experimentally validate their approach, proving the accuracy of strain gauge methods in fracture mechanics. In 1990, Berger *et al.* [4] developed a dynamic strain gauge technique to quantify SIFs in cracks that were propagating in a plate. They laid the groundwork for subsequent experimental developments in fractured mechanics by creating an algorithm to identify the crack tip and calculate the strain field. During the same time, Kuang and Chen [5] highlighted the importance of asymptotic strain expansions to lower measurement errors by proposing a single strain gauge approach to measure SIF in Mode I condition.

By comparing experimental findings with FE solutions, Parnas *et al.* [6] investigated strain gauge approaches for measuring opening mode SIFs in more detail. Due to local plastic deformation close to the fracture tip and finite gauge size effects, their investigation brought to light the shortcomings of conventional strain gauge techniques. An experimental technique for calculating SIFs resulting from residual stress was provided by Schindler *et al.* [7]. Their strategy made use of the crack compliance method, which computed SIF by inserting a tiny slit into a stressed component and monitoring strain changes. This technique offered a straightforward approach to calculate SIFs without the need for previous residual stress measurements.

A strain gauge technique was carried out by Kondo *et al.* [8] to determine the stress intensities of sheets with acute notches. Strong agreement between experimental and theoretical results was demonstrated by their work, which used the two-dimensional (2D) theory of elasticity to build a method that accurately estimated stress intensities in notch fracture mechanics. To increase the precision of Mode I SIF measurements, Kaushik *et al.* [9] looked at strain gauge placement strategies. Their study suggested a way to figure out the ideal strain gauge placement for precise SIF evaluation and underlined the significance of radial distance in guaranteeing legitimate strain gauge locations. For intricate designs, strain gauge methods were further improved by Swamy *et al.* [10]. They compared experimental SIF values with FE solutions while studying fully finite edge-cracked plates under tensile stress. They proved that, when used appropriately, strain gauge measurements yielded precise SIF values, confirming the usefulness of these methods in engineering applications.

To ensure accurate SIF calculations, Sarangi *et al.* [11] created an FE-based methodology for identifying the upper bound of valid strain gauge positions. Their research showed that the maximum allowable radial position of strain gauges is influenced by the fracture length-to-width ratio. Later, by presenting an FE-based technique for finding exactly the ideal

strain gauge placement for eccentric cracked topologies, Sarangi *et al.* [12] built on previous studies. The impact of fracture length-to-width ratio and model size on the ideal strain gauge placement was examined in their study. The results showed that the measurement accuracy of Mode I SIF is strongly influenced by both model size and crack shape. Especially for asymmetric crack patterns, their method increased the accuracy of strain gauge-based SIF estimation. By suggesting an experimental method for mixed-mode SIF measurement, another study by Sarangi *et al.* [2] built on this and improved strain gauge techniques for isotropic and composite materials. A sophisticated experimental method for figuring out Mode I SIF in orthotropic materials was presented by Sarangi *et al.* [13], highlighting the significance of strain gauge orientation and placement.

Chakraborty *et al.* [14] made substantial progress by introducing a novel single-strain gauge approach designed especially for orthotropic composite materials. Their results demonstrated a considerable improvement in measurement accuracy with an optimal strain gauge location inside a valid region. An ideal strain gauge placement technique for figuring out Mode I SIF in orthotropic laminates was created by Chakraborty *et al.* [15]. To find the ideal radial site for strain gauge placement, their study expanded on the Dally-Sanford (DS) technique and included FE analysis, greatly increasing measurement accuracy. Chakraborty *et al.* [16] expanded on this work by tackling several important problems with strain gauge-based SIF calculation. By applying earlier methods to mixed-mode fracture scenarios, they brought forth an improved methodology for identifying valid strain gauge locations. Their research improved the applicability of single and multiple strain gauge systems for both isotropic and orthotropic materials by resolving long-standing issues with radial orientation.

Generalized stress intensity parameters of sharp V-notched plates under transverse bending are calculated using strain gauges [17]. Using the fracture tip stresses determined by the strain gauge, the proportional extrapolation technique is given for correctly and experimentally determining SIFs [18]. A method for determining the Mode II SIFs using strain gauges has been well performed by Talha *et al.* [19]. To overcome the drawbacks of single-strain-gauge methods for measuring Mode I SIF in orthotropic composites, Mejni and Talha [20] have recently proposed and validated two new dual-strain-gauge methods that improve accuracy in complex strain gradient and localized plasticity conditions. Mode I notch SIFs for sharp V-notched designs may be efficiently and effectively determined using a verified single-strain-gauge method; the results emphasize the significance of correct gauge positioning to prevent inaccurate measurements [21].

A stain gauge technique always places importance on measuring the strain on the structure. Based on recent studies strain gauge technique is utilized with an advanced artificial intelligence technique to highly predict the strain values. Li *et al.* [22] implemented impact-loading tests on granite and polymethyl methacrylate specimens using acute and obtuse angle strain gauges, tracking crack propagation velocities and Mode I SIFs while validating their gauge-based measurements against caustic imaging techniques. Feng and Qian [23] developed an adaptive-learning scheme that fuses strain-relaxation data with crack-front geometry in welded plate joints – employing a regression neural network and modified bootstrap particle filter to sequentially update crack sizes, thereby advancing a digital twin-driven fatigue-life estimation method. Yoon *et al.* [24] introduced a hybrid deep neural network plus principal component analysis strategy for real-time structural health monitoring using a sparse array of 12 strain gauges. Their system reconstructs the full-field strain profile and enables precise crack detection/localization in carbon fiber reinforced polymer under cyclic four-point bending. Shah Mansouri *et al.* [25] demonstrated an machine learning-based structural health monitoring system utilizing a minimal Bluetooth-linked strain gauge network. By applying Shewhart charts, Grubbs' test, and hierarchical clustering, they achieve real-time crack detection and localization in 2- and 4-point bending experiments with as few as five sensors. Cheok *et al.* [26] proposed a strain-data-driven digital twin capable of calculating ΔJ integrals directly from strain measurements in crack-interfaced welded plate joints. This enables modeling fatigue crack growth under variable loading in the elasto-plastic regime and supports accurate remaining-life estimation. Zhao *et al.* [27] presented an end-to-end digital-twin-style learning framework that combines dimensionality reduction, neural networks, and a path-slicing and re-weighting scheme to predict fatigue crack trajectories and life remaining under uncertainties.

While previous research by Sarangi *et al.* [11,12] and Chakraborty *et al.* [14–16] have contributed significantly to understanding strain gauge placement in composite and orthotropic materials, a specific research gap remains for isotropic metallic materials, particularly aluminum, in edge-cracked configurations. Moreover, most existing studies focus on single crack lengths or overlook the effect of varying a/W ratios on $r_{\max}$ determination. The aim of this study is to fill this gap by systematically analyzing the impact of a/W ratios on optimal strain gauge locations using FE modeling. Additionally, this work uniquely integrates mesh convergence studies into the $r_{\max}$ evaluation process to improve SIF accuracy, an approach not explicitly detailed in earlier literature.

3 Radial location of strain gauge: Determination of r_{max}

The DS technique was applied to determine the Mode I SIF for precise r_{max} value measurement [28]. The strain gauge should be positioned as far away from the crack tip as feasible while being within the r_{max}, according to the DS approach. Because of plasticity, strain gradients, and 3D effects, the measured strains may be significantly impacted if the gauge is placed close to the crack tip [12]. SIFs are then calculated by comparing the measured strains to theoretical values valid inside the specified zone. As a result, the region around a crack tip is separated into three zones: zone I, zone II, and zone III, as seen in Figure 1.

Zone I is near the crack tip, and the first term of the strain series (single strain term) is adequate to represent the strains in this zone. However, it is not a valid zone for reliable strain measurement since the stress state in this region is three-dimensional (3D), and the recorded strains will be heavily influenced by plasticity effects. Furthermore, the errors in measuring the position of the strain gauge are high if it is placed close to the crack tip. Zone III is not suited for strain data collecting because correct findings require a high number of terms in the strain series. As a result, the intermediate region, or zone II, is the most suitable and optimal zone for accurately measuring surface strains. This is defined as a zone in which the strain field may be accurately described using a single element and a small number of higher-order terms.

The generalized Westergaard approach can be used to obtain expressions for various strain components within zone II. The modified airy stress function in this technique is given by [28]

$$\varnothing = \mathrm{Re}\bar{\bar{Z}}(z) + y\mathrm{Im}\bar{Z}(z) + y\mathrm{Im}\bar{Y}(z), \tag{1}$$

where

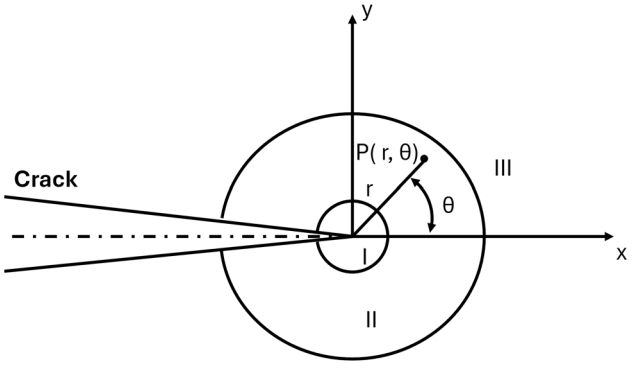

Figure 1: Various regions at the crack.

$$\frac{d\bar{\bar{Z}}}{dz} = \bar{Z}, \quad \frac{d\bar{Z}}{dz} = Z, \text{ and} \frac{d\bar{Y}}{dy} = Y, \tag{2}$$

and the complex analytic functions $Z(z)$ and $Y(z)$ are defined as

$$Z(z) = \sum_{n=0}^{\infty} A_n z^{n-\frac{1}{2}} = \frac{K}{\sqrt{2\pi z}} + \sum_{n=1}^{\infty} A_n z^{n-\frac{1}{2}}, \tag{3}$$

$$Y(z) = \sum_{m=0}^{\infty} B_m z^m = \frac{\sigma_{0x}}{2} + \sum_{m=1}^{\infty} B_m z^m, \tag{4}$$

which are functions of the series type with an unlimited number of coefficients (A_1; A_2; _ _ _; A_n; B_1; B_2; _ _ _; B_n) that can be found using the problem's boundary conditions. The domain-wide stress components are represented by

$$\begin{aligned} \sigma_{xx} &= \mathrm{Re}Z - y\mathrm{Im}\acute{Z} - y\mathrm{Im}\acute{Y} + 2\,\mathrm{Re}Y \\ \sigma_{yy} &= \mathrm{Re}Z + y\mathrm{Im}\acute{Z} + y\mathrm{Im}\acute{Y} \\ \tau_{xy} &= -y\,\mathrm{Re}\acute{Z} - y\,\mathrm{Re}\acute{Y} - \mathrm{Im}Y \end{aligned}. \tag{5}$$

Equations for the strain field, assuming planar stress conditions, can be found as

$$\begin{aligned} E\varepsilon_{xx} &= (1-\nu)\,\mathrm{Re}Z - (1+\nu)y\mathrm{Im}\acute{Z} - (1+\nu)y\mathrm{Im}\acute{Y} \\ &\quad + 2\,\mathrm{Re}Y \\ E\varepsilon_{yy} &= (1-\nu)\,\mathrm{Re}Z + (1+\nu)y\mathrm{Im}\acute{Z} + (1+\nu)y\mathrm{Im}\acute{Y} \\ &\quad + 2\nu\,\mathrm{Re}Y \\ E\gamma_{xy} &= 2(1+\nu)(-y\,\mathrm{Re}\acute{Y} - \mathrm{Im}Y - y\,\mathrm{Re}\acute{Z}) \end{aligned}. \tag{6}$$

The strain field in the domain with an unlimited number of unknown coefficients, A_n and B_m, can be precisely represented by substituting the series form of complex functions $Z(z)$ and Y(z) from Eqs. (3) and (4). It is expected that the three-parameter series with unknown coefficients, A_0, A_1, and B_0, may adequately represent the strain field in zone II [28]. Thus, the strain field's three-term representation in this zone is

$$\begin{aligned} 2G\varepsilon_{xx} &= A_0 r^{-1/2}\cos\frac{\theta}{2}\left[k - \sin\frac{\theta}{2}\sin\frac{3\theta}{2}\right] + \frac{2B_0}{(1+\nu)} \\ &\quad + A_1 r^{1/2}\cos\frac{\theta}{2}\left[k + \sin^2\frac{\theta}{2}\right] \\ 2G\varepsilon_{yy} &= A_0 r^{-1/2}\cos\frac{\theta}{2}\left[k + \sin\frac{\theta}{2}\sin\frac{3\theta}{2}\right] - \frac{2\nu B_0}{(1+\nu)} \\ &\quad + A_1 r^{1/2}\cos\frac{\theta}{2}\left[k - \sin^2\frac{\theta}{2}\right] \\ 2G\gamma_{xy} &= A_0 r^{-1/2}\left[\sin\theta\cos\frac{3\theta}{2}\right] - A_1 r^{1/2}\cos\frac{\theta}{2}\left[\sin\theta\cos\frac{\theta}{2}\right] \end{aligned}. \tag{7}$$

where the unknown coefficients $k = (1-\nu)/(1+\nu)$ and A_0, A_1, and B_0. It can be found by using geometry and the loading circumstances of the sample. It may be demonstrated using the definition of K_1 that

$$K_1 = \sqrt{2\pi A_0}\,. \tag{8}$$

At point P, the strain component, $\varepsilon_{\acute{x}\acute{x}}$, which is identified by r and θ (Figure 2), is provided by

$$\begin{aligned} 2G\varepsilon_{\acute{x}\acute{x}} = {} & A_0 r^{-1/2}\left[k\cos\frac{\theta}{2} - \frac{1}{2}\sin\theta\sin\frac{3\theta}{2}\cos 2\alpha\right. \\ & \left. + \frac{1}{2}\sin\theta\cos\frac{3\theta}{2}\sin 2\alpha\right] \\ & + A_1 r^{1/2}\cos\frac{\theta}{2}\left[k + \sin^2\frac{\theta}{2}\cos 2\alpha\right. \\ & \left. - \frac{1}{2}\sin\theta\sin 2\alpha\right] + B_0(k + \cos 2\alpha). \end{aligned} \tag{9}$$

The angle α can be chosen so that the coefficient B_0 in Eq. (9) is removed.

$$\cos 2\alpha = -k = \frac{1-\nu}{1+\nu}. \tag{10}$$

Likewise, the coefficient A_1 can be set to zero if the angle θ is chosen as

$$\tan\frac{\theta}{2} = -\cot 2\alpha. \tag{11}$$

Therefore, the strain, $\varepsilon_{\acute{x}\acute{x}}$, which is in turn related to K_1, can be measured by putting a single strain gauge with α and θ as indicated (Figure 2) by Eqs. (10) and (11).

$$\begin{aligned} 2G\varepsilon_{\acute{x}\acute{x}} = {} & \frac{K_1}{\sqrt{2\pi r}}\left[k\cos\frac{\theta}{2} - \frac{1}{2}\sin\theta\sin\frac{3\theta}{2}\cos 2\alpha\right. \\ & \left. + \frac{1}{2}\sin\theta\cos\frac{3\theta}{2}\sin 2\alpha\right]. \end{aligned} \tag{12}$$

The equation, which may be expressed as follows, precisely calculates $\varepsilon_{\acute{x}\acute{x}}$ up to a radial distance of $r_{\max}$:

$$\begin{aligned} \varepsilon_{\acute{x}\acute{x}} = {} & \frac{1}{\sqrt{r}}\left[\frac{K_1}{G\sqrt{8\pi}}\left(k\cos\frac{\theta}{2} - \frac{1}{2}\sin\theta\sin\frac{3\theta}{2}\cos 2\alpha\right.\right. \\ & \left.\left. + \frac{1}{2}\sin\theta\cos\frac{3\theta}{2}\sin 2\alpha\right)\right]. \end{aligned} \tag{13}$$

Within the square bracket on the right side of Eq. (13) is a constant for a given configuration, applied load, Poisson's ratio ν, and Young's modulus E. Consequently,

$$\varepsilon_{\acute{x}\acute{x}} = \frac{C}{\sqrt{r}}. \tag{14}$$

C is constant in this case. Calculating the logarithm of each side of Eq. (14)

$$\ln(\varepsilon_{\acute{x}\acute{x}}) = -\frac{1}{2}\ln(r) + \ln(C). \tag{15}$$

Eq. (11) provides the line along which Eq. (15) is valid for $r \le r_{\max}$. Plotting Eq. (15) on the −log axes shows a straight line with an intercept of ln(C) and a slope of −0.5. The straight-line property should theoretically collapse beyond $r > r_{\max}$ because Eq. (9) requires more than three parameters to predict $\varepsilon_{\acute{x}\acute{x}}$. The value of $r_{\max}$ can be precisely determined from the –log plots of $\varepsilon_{\acute{x}\acute{x}}$ and r using the straight-line property displayed by Eq. (15). It should be highlighted that a trustworthy method is required for the precise identification of the straight-line endpoint in Eq. (15) due to logarithmic displays.

4 Problem definition

The mechanical integrity and failure behavior of structural components, especially aluminum plates, are greatly impacted when they have an edge fracture [29,30]. The material defined for the aluminum plate has a Young's

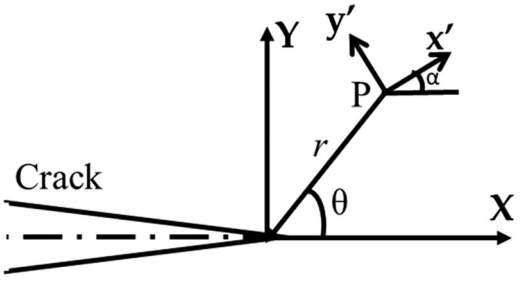

Figure 2: Strain gauge location and orientation.

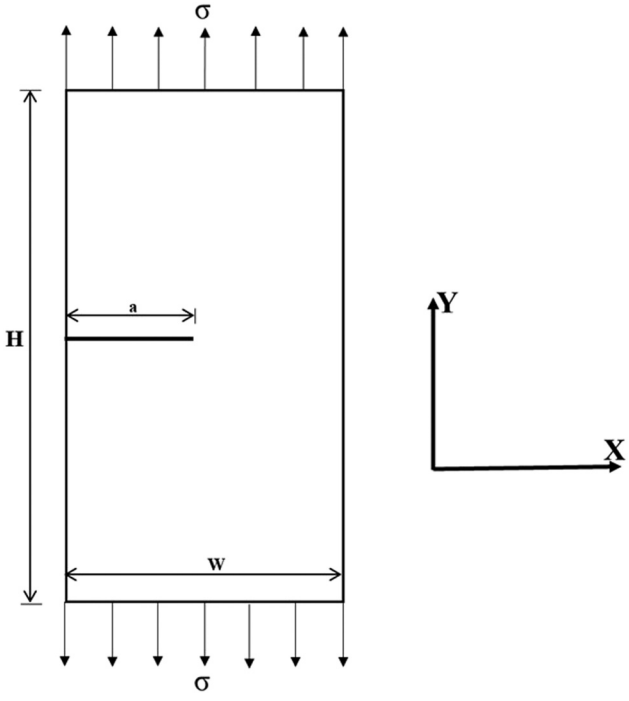

Figure 3: Edge-cracked aluminum plate.

Table 1: Dimensions of the edge-cracked plates

Parameters (mm)	Configuration 1	Configuration 2	Configuration 3
H	220	220	220
W	35	25	40
a	12.5	8.5	10.0
a/*W*	0.357	0.34	0.25

modulus of 68.95 GPa, a Poisson's ratio of 0.33, and a density of 2,715 kg/m^3 [31]. A single-ended edge-cracked aluminum plate subjected to uniaxial tensile stress is shown in Figure 3, where the fracture response is influenced by critical factors including crack length (*a*), plate width (*W*), and height (*H*). Dimensions for three distinct configuration examples are shown in Table 1, with *W* varying while *H* stays constant. A comparative analysis is necessary because the three configurations differ somewhat in the *a*/*W* ratio, which controls the SIF and crack propagation behavior. Understanding failure causes and placing strain gauges optimally for accurate readings depend on the experimental determination of SIFs for these fractured designs.

The goal of the current work is to identify the optimum strain gauge placement for precisely measuring the SIF in aluminum plates with single-edge cracks (Figure 4). The study employs numerical simulations to assess how crack length (*a*) and plate width (*W*) affect fracture behavior and strain distribution under applied tensile loads. Finding appropriate strain gauge locations is essential for reducing measurement errors and guaranteeing accurate SIF determination because different configurations have different *a*/*W* ratios. In thin metallic constructions, the results will help validate numerical models for fracture analysis.

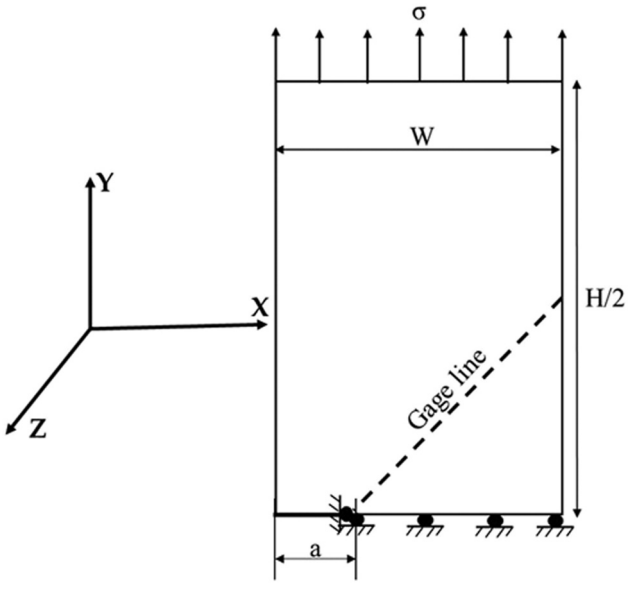

Figure 4: Applied boundary conditions for the edge-cracked plate.

The present study considered theoretical expressions that were previously presented for edge-cracked plates subjected to uniform uniaxial tensile load; it also demonstrates the geometric parameter and material properties of the edge-cracked plate, respectively, which were used multiple times in the current studies; it presented the determination of $r_{\max}$ based on the theoretical expression in conjunction with FE analysis for the prepared sample (edge-cracked plate); and it uses a gauge line at a specific angle concerning the fracture mechanics study to investigate $r_{\max}$ for three configuration models.

5 FE modeling

Because it can model irregular meshes and provide high accuracy in SIF computations, the PLANE183 design element was selected for the FE analysis of edge-cracked aluminum plates in this study. Unlike lower-order elements like PLANE182 (four-node), which use linear shape functions, PLANE183 uses quadratic shape functions, which improve the ability to capture stress gradients near crack tips. The ability to include mid-side nodes, which raises the precision of displacement and strain field approximations, is one of the main advantages of the element. This characteristic is particularly helpful in areas where stress singularities form, like crack tips, where there is a large concentration of stress. The mid-side nodes of PLANE183 elements were moved to the quarter-point location following accepted fracture mechanics modeling procedures to precisely model the singularity at the crack tip. SIFs may be precisely determined thanks to this quarter-point approach, which guarantees that the $1/\sqrt{r}$ singularity is accurately simulated [32]. Furthermore, PLANE183 is appropriate for elastic-plastic fracture mechanics simulations where material yielding may occur near the crack tip since it allows nonlinear material behavior. When examining aluminum plates under heavy loads, this ability is

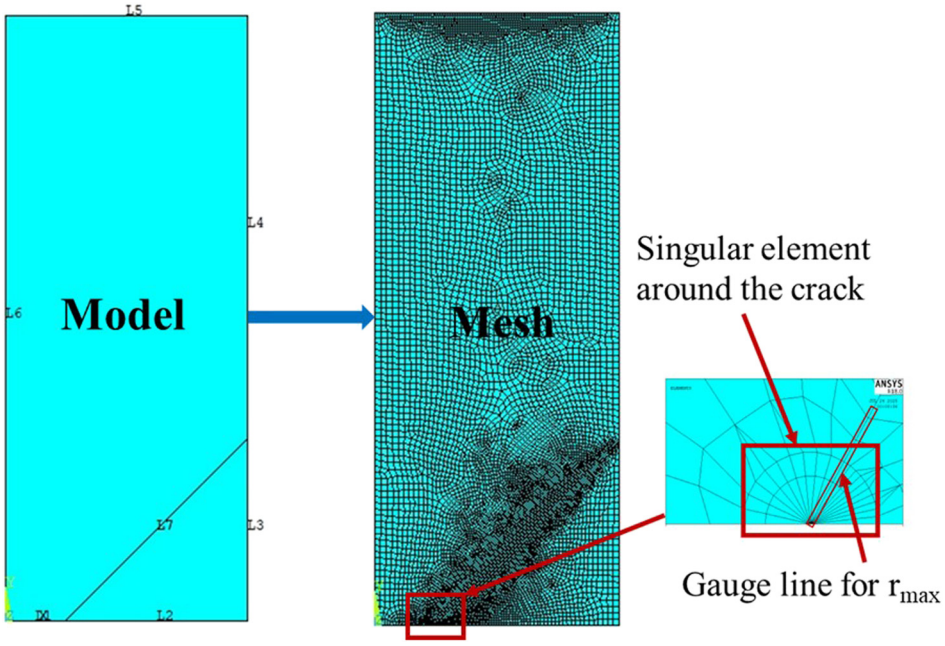

Figure 5: The FE model with meshing.

essential for effectively capturing the effects of both elastic and plastic deformation.

As shown in Figure 5, line 7 has a spider-web meshing pattern that was used in this study to enhance solution convergence and preserve numerical stability around the crack tip using collapsed PLANE183 components. Line 7 has been initiated from the crack tip, and the crack has singular elements, which cannot be seen in the normal image of the plate. Therefore, the zoom view of the crack has been extracted to observe the singular element and the gauge line, which is line 7, for a thorough understanding. To compare the accuracy and computing efficiency of SIF, mesh refinement studies were carried out using different coarse, medium, and fine mesh densities. This method improved the dependability of experimental validation by guaranteeing that the ideal strain gauge site was identified with the fewest possible numerical errors. Therefore, the PLANE183 element used in this study was crucial for obtaining high-fidelity stress and strain predictions, which are necessary for fracture analysis and evaluating the structural integrity of cracked aluminum plates.

As reported in Table 1, samples with edge cracks of three distinct lengths were subjected to the numerical method for calculating $r_{\max}$ in fractured plates using the FE method. Three mesh densities with a/W ratios of 0.357, 0.34, and 0.25 were used for each sample in convergence research to assess the impact of mesh sensitivity on $r_{\max}$ values. To evaluate their influence on the outcomes, the number of elements (NE) and nodes (NN) associated with each mesh arrangement were also noted.

5.1 Analysis

As seen in Figures 4 and 5, the mesh size is such that the nodes of many elements fall along the radial line, creating an angle of θ with the axis of the crack according to Eq. (13). The gauge line leaves the edge-cracked plate at its external boundaries after beginning at the tip of the crack. According to the DS technique [28], to measure the linear strain, ε_{aa}, as depicted in Figure 4, a single strain gauge must be positioned at an appropriate location on this line in the direction of α using Eq. (3). The linear strain, ε_{aa}, in the direction indicated by α is then obtained from the computed strains in the global coordinates concerning the gauge line.

The radial distances (r) between each node on the gauge line and the crack tip are then determined. Table 2 displays three mesh sizes for each configuration plate, and a sample of mesh can be seen in Figure 6. The radius at the crack point is 0, hence it is not considered in charts. It is interesting to note that in all three examples, each scenario has a distinct linear section followed by a nonlinear portion (in logarithmic scale), as anticipated by theory in the prior study. The linear trend is visible up to a certain radial distance and then gradually shifts to the nonlinear section.

Table 2: Mesh size of each plate

Mesh size	Configuration 1 (a/b = 0.357)		Configuration 2 (a/b = 0.34)		Configuration 3 (a/b = 0.25)	
	NE	NN	NE	NN	NE	NN
Size 1 (coarse)	666	1,972	447	1,318	1,913	5,942
Size 2 (medium)	2,790	8,379	2,394	7,253	5,023	15,384
Size 3 (fine)	8,012	24,097	6,951	20,998	11,364	34,481

6 Results in discussion

This section extracted the results of different configurations of plates for the optimum location of the strain gauge through the inclined line from the crack tip at an angle of 45 degrees. The current investigation used the DS technique based on the straight-line part that identifies the initial fatal point. This technique initially used a line with a slope of −0.5, which was superimposed on the plots of $\ln(\varepsilon_{\dot{x}\dot{x}})$ *vs* $\ln(r)$. Then, the slope line was used to calculate the exact value and total relative error in percentage using the formula $\ln(\varepsilon_{\dot{x}\dot{x}})$. Finally, the radius variables were then assessed across the plot. Based on the current investigation, it has been observed that the error is greater in the nonlinear region and gradually lowers as one approaches the corresponding point in the line of Eq. (16).

$$\ln(\varepsilon_{x'x'}) = -\frac{1}{2}\ln(r) + \ln(C). \tag{16}$$

The superposed line was utilized to determine the $r_{\max}$ or point of deviation of the log-log plot, with an error of 0.5%. Eq. (5) represents the recommended approach for $r_{\max}$ evaluation.

6.1 Configuration 1

For configuration 1, Figure 7 shows the obtained $r_{\max}$ values, which represent the validity extent of the three-parameter zone. Each plate has a unique a/W ratio, which influences the gauge line distance because $r_{\max}$ varies appropriately. As a result, this study obtains findings by altering the a/W ratio to determine the ideal location of $r_{\max}$. Furthermore, the simulation models allow for mesh size modifications, giving you more freedom when studying different mesh combinations. To optimize the strain gauge placement, each plate was evaluated with three different mesh densities. Mesh sizes and names have previously been set for each plate in this study (Table 2).

Figure 7 shows how mesh refinement has a substantial impact on the estimate of $r_{\max}$, illustrating that finer mesh densities result in more precise estimations of the three-parameter zone. Variation in $\ln(\varepsilon_{\dot{x}\dot{x}})$ *vs* $\ln(r)$ over mesh sizes shows a transition between linear and nonlinear behavior, validating the three-parameter validity of the zone. This emphasizes the importance of mesh convergence studies

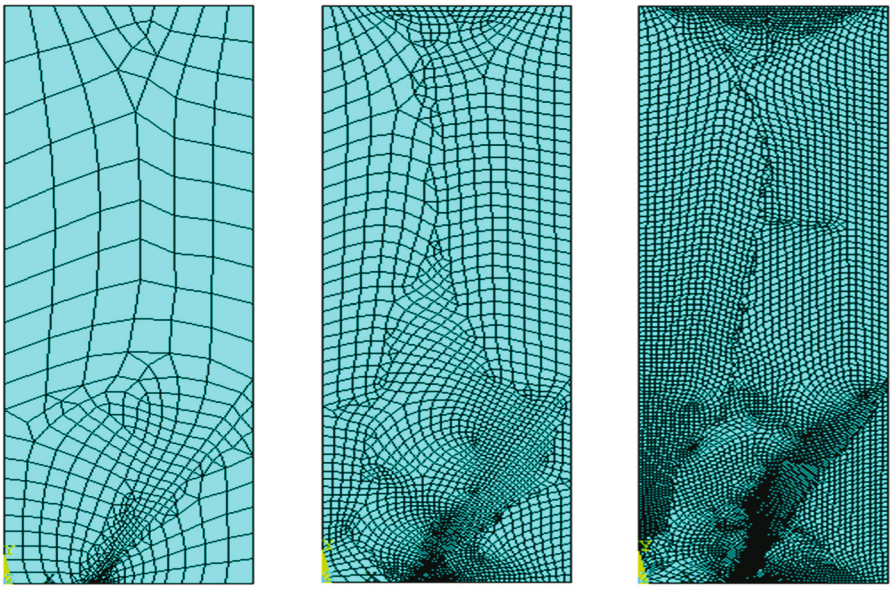

(a) (b) (c)

Figure 6: Different FE meshes for a/b = 0.357. (a) NE = 666, NN = 1,975. (b) NE = 2,790, NN = 8,379. (c) NE = 8,012, NN = 24,097.

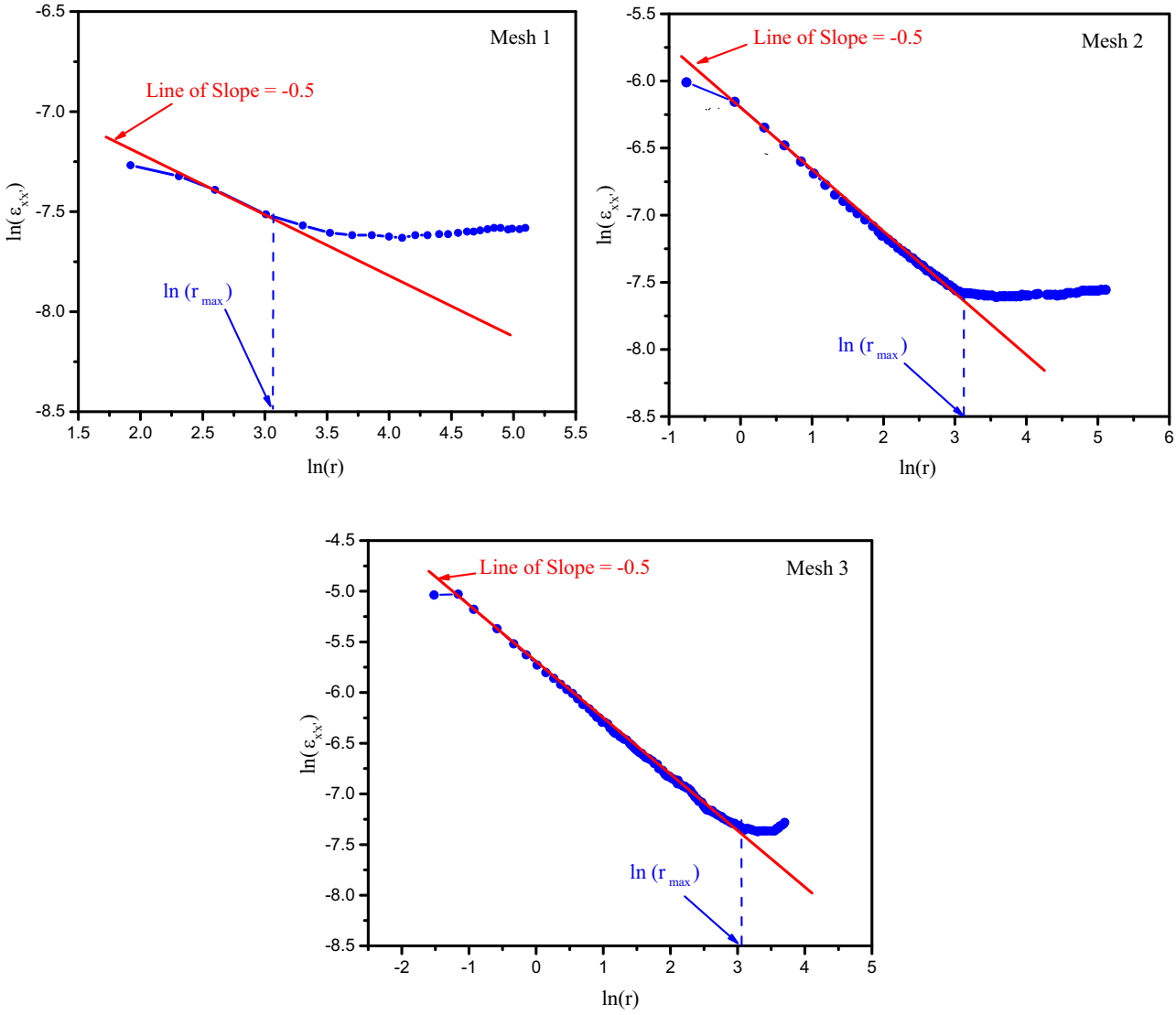

Figure 7: Linear and nonlinear variation in $\ln(\varepsilon_{\dot{x}\dot{x}})$ *vs* $\ln(r)$ along the gauge line for the sequence of meshes of the edge-cracked plate with $a/W = 0.357$.

for achieving accurate strain gauge placement. Moreover, the variation in $r_{\max}$ values with varied a/W ratios emphasizes the significance of adjusting strain gauge placements for accurate SIF estimation. The study further confirms that, beyond a given level of mesh refinement, no additional advances in $r_{\max}$ or SIF values occur, showing numerical convergence. These findings highlight the need for systematic FE modeling to balance computational efficiency and ensure high-accuracy predictions in fracture mechanics analyses.

6.2 Configuration 2

Figure 8 depicts the linear and nonlinear fluctuations in ln $(\varepsilon_{\dot{x}\dot{x}})$ *vs* ln(r) along the gauge line for different mesh densities in configuration 2 (a/b = 0.34). Like configuration 1, this graphic demonstrates how mesh refinement affects the $r_{\max}$ estimate and the validity of the three-parameter zone.

The graphs for all meshes show how $r_{\max}$ values change as the mesh density increases. The coarser mesh (mesh 1) causes more pronounced nonlinearity, resulting in higher variations in strain calculations around the gauge line. The transition from linear to nonlinear behavior happens early, implying a less accurate calculation of $r_{\max}$ due to low mesh resolution. Mesh 2 of the revised mesh enhances the precision of the strain distribution, resulting in a longer linear region before transitioning into the nonlinear zone. This shows that the strain field is better captured, although slight errors in estimating $r_{\max}$ remain. Mesh 3, the finest mesh, shows a well-defined linear trend in the $\ln(\varepsilon_{\dot{x}\dot{x}})$ *vs* $\ln(r)$ plot, closely matching the expected slope of −0.5. The shift into the nonlinear

region happens at a greater distance, implying that the three-parameter zone is better captured. The projected r_{max} value from mesh 3 is more dependable than the coarser meshes, emphasizing the importance of mesh refinement in numerical SIF estimation.

Comparing the results to configuration 1 (a/W = 0.357), as the a/b ratio varies, so do the associated gauge line distance and r_{max} location. The findings indicate that a more refined FE mesh is necessary for lower a/b ratios to obtain convergence in r_{max} determination. Furthermore, the final revised meshes, which show no further improvement in r_{max} values, are important in assuring precise strain gauge placement for experimental validation. Thus, the results of configuration 2 reinforce the need to complete mesh convergence studies and adjust gauge line distances based on a/W ratios, ensuring accurate r_{max} estimation and dependable SIF determination in FE analyses.

6.3 Configuration 3

Figure 9 shows the linear and nonlinear fluctuations in ln ($\varepsilon_{\acute{x}\acute{x}}$) *vs* ln($r$) along the gauge line for different mesh densities (mesh 1–3). Figure 9 shows how mesh refinement affects the estimation of r_{max} and the size of the three-parameter zone, like configurations 1 and 2, but with noteworthy variations due to the lower a/W ratio.

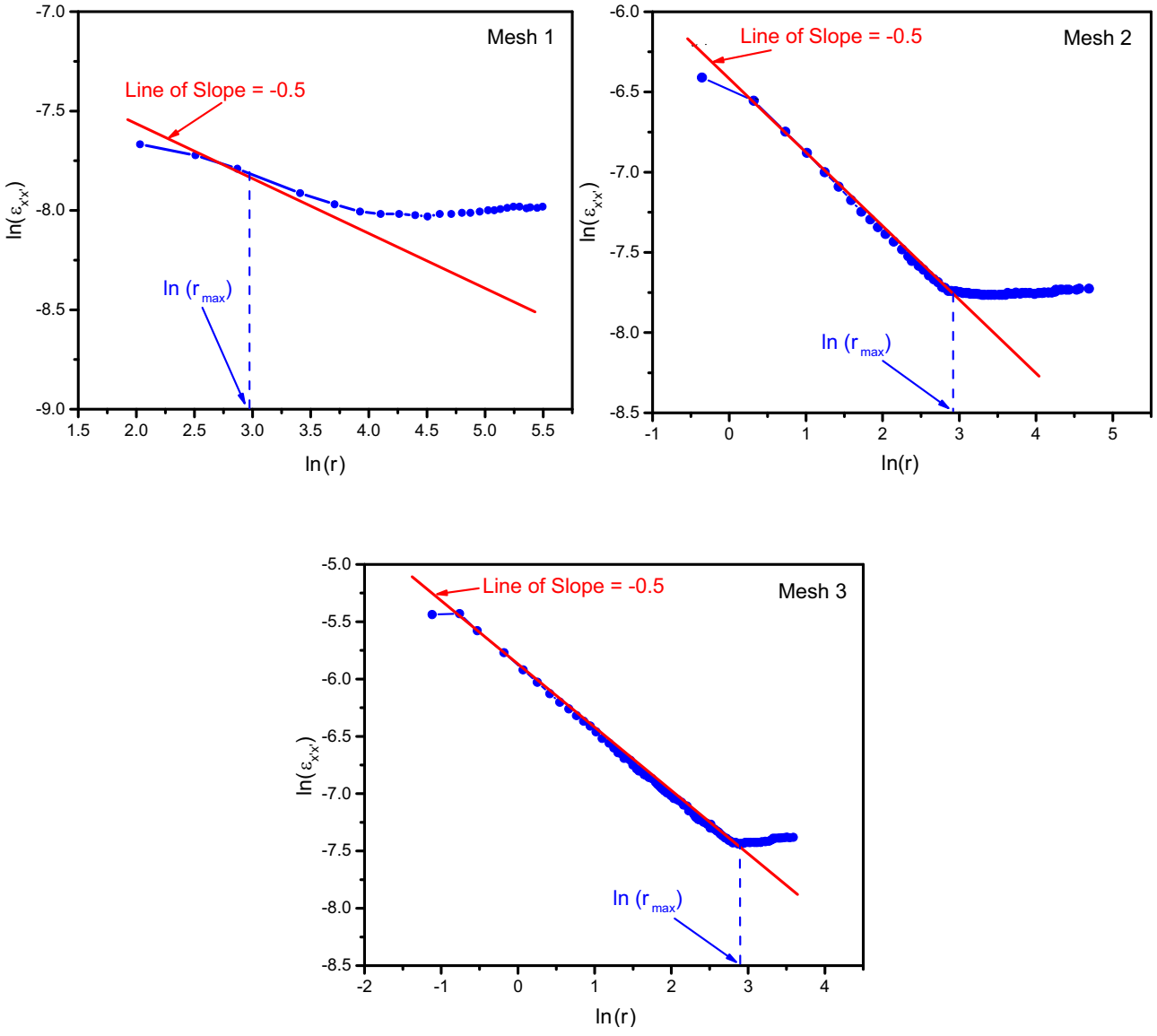

Figure 8: Linear and nonlinear variation in ln($\varepsilon_{\acute{x}\acute{x}}$) *vs* ln($r$) along the gauge line for the sequence of meshes of the edge-cracked plate with a/W = 0.34.

In mesh 1 (coarse mesh), the shift from linear to nonlinear strain behavior occurs at a shorter ln(r) distance, showing that a coarser mesh does not fully capture the three-parameter zone. The small number of pieces causes deviations from the predicted −0.5 slope earlier than with finer meshes, resulting in a less accurate estimate of r_{max}. For mesh 2 (medium mesh), the refinement enhances strain distribution accuracy, resulting in a longer linear region before shifting to the nonlinear zone. The ln(r) value has changed relative to mesh 1, indicating a more credible estimate. However, certain deviations from the expected slope exist, indicating that further adjustment is required for optimal accuracy. Mesh 3 (fine mesh) shows the most refined linear trend in the ln($\varepsilon_{\hat{x}\hat{x}}$) *vs* ln($r$) plot, closely matching the expected slope of −0.5. The shift into the nonlinear region occurs at a greater radial distance, indicating that finer meshes better capture the three-parameter zone. The projected r_{max} value in this scenario is the most dependable of the three, highlighting the significance of fine meshing in numerical strain gauge optimization.

When compared to configurations 1 (a/W = 0.357) and 2 (a/W = 0.34), configuration 3 has a significantly larger valid r_{max} zone due to its lower a/W ratio. The wider plate width and shorter fracture length result in a less steep strain gradient, necessitating finer meshes to accurately calculate r_{max}. This demonstrates that as a/W declines, the necessary mesh refinement increases to reflect the genuine strain of behavior. As a result, the findings of configuration 3

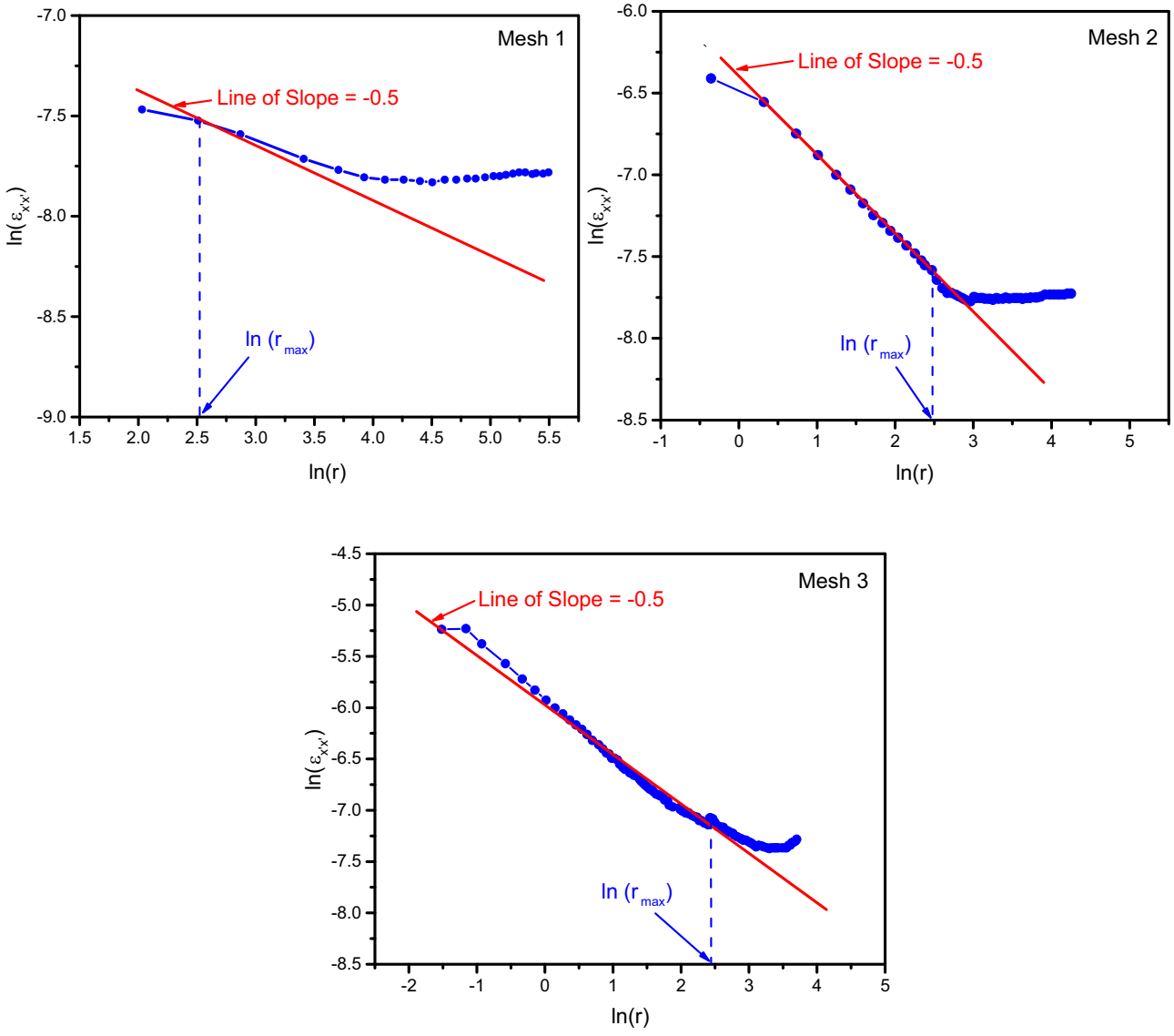

Figure 9: Linear and nonlinear variation in ln($\varepsilon_{\hat{x}\hat{x}}$) *vs* ln($r$) along the gauge line for the sequence of meshes of the edge-cracked plate with a/W = 0.25.

highlight the significance of mesh convergence research in fracture mechanics. The investigation demonstrates that beyond a particular mesh refinement level, no further increase in r_{max} and SIF estimation is found. This validates the final refined mesh as best for strain gauge placement and SIF calculations.

6.4 Comparison of all samples

The results in Table 3 show how r_{max} values converge with mesh refinement for various a/W ratios. As shown, r_{max} drops as mesh size decreases, demonstrating that mesh refinement has a major impact on the valid measurement zone for strain gauges. For a/W = 0.357, mesh 1 has an initial r_{max} value of 23.33 mm, which decreases to 20.29 mm. When the mesh size is high, mesh 3 is used, indicating a definite convergence trend. A similar pattern is observed with a/W = 0.34, with r_{max} decreasing from 18.17 mm (mesh 1) to 17.51 mm (mesh 3). The same tendency is observed for a/W = 0.24, where r_{max} decreases from 13.12 to 12.16 mm as mesh density increases. These findings demonstrate that when the a/W ratio declines, so does r_{max}, implying that finer meshes are required to accurately capture the three-parameter zone. Furthermore, the slight differences in r_{max} between meshes 2 and 3 demonstrate that beyond a certain level of refinement, additional mesh increases give negligible improvement, emphasizing the necessity of mesh convergence studies in fracture mechanics simulations.

6.5 Validation of the current method

The current FE analysis of r_{max} values for the edge-cracked plate was compared to the results of Sarangi *et al.* [12] for a/W = 0.34 and 0.357. As demonstrated in Figure 10, the current results and Sarangi *et al.* [12] results are nearly identical, with a relative error of less than 3%, which can be seen in Table 4.

Table 3: Model configuration

Mesh size	r_{max} (mm)		
	a/W = 0.357	a/W = 0.34	a/W = 0.24
Mesh size 1	23.33	18.17	13.12
Mesh size 2	20.90	17.81	13.08
Mesh size 3	20.29	17.51	12.16

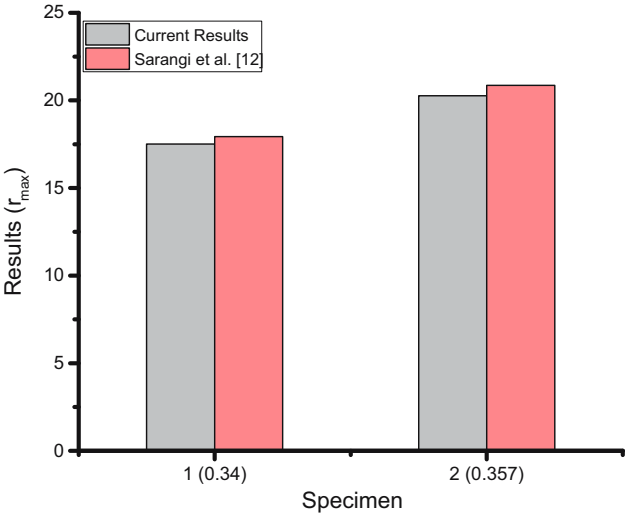

Figure 10: Comparison of results.

Table 4: Comparison of current work and relative error

Specimen	r_{max} (mm) Current results	r_{max} (mm) Sarangi *et al.* [12]	Relative error %
1 (0.34)	17.51	17.93	2.342
2 (0.357)	20.26	20.86	2.876

This validates the existing numerical accuracy of the model in calculating r_{max} for edge-cracked plates. It is important to note that Sarangi *et al.* [12] did not examine a/W = 0.25; hence, validation could only be performed for the two samples (a/W = 0.34 and 0.357). The present samples were created using the existing model, assuring consistency in methodology and allowing for direct comparisons between the two subjects of research. The minimal changes between the results are due to mesh refinement modifications, numerical discretization, and tiny computing differences in the FE modeling approach. Nonetheless, the significant agreement between the two investigations supports the existing approach for strain gauge placement and r_{max} estimation in the research of fracture mechanics.

7 Conclusion and recommendations

Using numerical modeling, this work successfully found the best strain gauge placement for measuring SIF in single-ended fractured aluminum plates with three

different configurations. The investigation indicated that r_{max}, the maximum valid radial position for strain measurements, is substantially influenced by the a/W ratio and mesh refinement level. The findings revealed that positioning strain gauges too close to the crack tip produces errors due to plasticity effects, while placing them too far away causes a loss of sensitivity to the singularity-dominated strain field. Mesh convergence research revealed that after a certain level of mesh refinement, more refinement produces a modest gain in r_{max} and SIF accuracy. The FE results were tested against experimental data, which revealed a relative error of less than 3%, validating the robustness of the suggested technique. This research extends the current understanding of strain gauge optimization by addressing configurations of aluminum plates with varying a/W ratios, which have been underrepresented in earlier work. Unlike prior studies that primarily focus on composite materials or fixed configurations, our study provides a generalized FE framework for r_{max} estimation across multiple edge-crack geometries. Furthermore, by incorporating a systematic mesh refinement analysis, this work enhances the precision of strain-based SIF measurements in isotropic materials, thereby contributing a novel methodology for fracture assessment in metallic structures.

As the current study attempted to discover the optimal strain gauge location for SIF examination using the FE approach, future research could consider confirming the same configurations of a thin aluminum plate with experimental results. Furthermore, this modeling technique can be applied to Mode II or mixed mode cracked plates and complex geometries to improve SIF determination methods. Finally, the same mixed-mode fracture models can be validated by experimental data.

Acknowledgments: This research was supported by the Structures and Materials (S&M) Research Lab of Prince Sultan University, and the authors acknowledge Prince Sultan University for paying the article processing charges (APC).

Funding information: Authors state no funding involved.

Author contributions: All authors have accepted responsibility for the entire content of this manuscript and approved its submission.

Conflict of interest: Authors state no conflict of interest.

Data availability statement: The datasets generated during and/or analyzed during the current study are available from the corresponding author on reasonable request.

References

[1] Aabid A, Hrairi M, Ali JSM, Sebaey TA. A review on reductions in the stress-intensity factor of cracked plates using bonded composite patches. Materials (Basel). 2022;15(3086):20.

[2] Sarangi H, Murthy KSRK, Chakraborty D. Optimum strain gage locations for accurate determination of the mixed mode stress intensity factors. Eng Fract Mech. 2012;88:63–78. doi: 10.1016/j.engfracmech.2012.04.006.

[3] Shukla A, Agarwal BD, Bhushan B. Determination of stress intensity factor in orthotropic composite materials using strain gages. Eng Fract Mech. 1989;32(3):469–77.

[4] Berger JR, Dally JW, Sanford RJ. Determining the dynamic stress intensity factor with strain gages using a crack tip locating algorithm. Eng Fract Mech. 1990;36(1):145–56.

[5] Kuang JH, Chen LS. A single strain gage method for K_I measurement. Eng Fract Mech. 1995;51(5):871–8.

[6] Parnas L, Bilir ÖG, Tezcan E. Strain gage methods for measurement of opening mode stress intensity factor. Eng Fract Mech. 1996;55(3):485–92.

[7] Schindler HJ, Cheng W, Finnie I. Experimental determination of stress intensity factors due to residual stresses. Exp Mech. 1997;37(3):272–7.

[8] Kondo T, Kobayashi M, Sekine H. Strain gage method for determining stress intensities of sharp-notched strips. Exp Mech. 2001;41(1):1–7.

[9] Kaushik B, Murthy KSRK, Robi PS. Determination of strain gage locations for the accurate measurement of opening mode stress intensity factors. J Mech Mater Struct. 2008:1757–71.

[10] Swamy S, Srikanth MV, Murthy KSRK, Robi PS. Determination of mode I stress intensity factors of complex configurations using strain gages. J Mech Mater Struct. 2006;1(Jan):97–127. http://pjm.math.berkeley.edu/jomms/2006/1-1/p05.xhtml.

[11] Sarangi H, Murthy KSRK, Chakraborty D. Optimum strain gage location for evaluating stress intensity factors in single and double ended cracked configurations. Eng Fract Mech. 2010;77(16):3190–203. doi: 10.1016/j.engfracmech.2010.08.003.

[12] Sarangi H, Murthy KSRK, Chakraborty D. Radial locations of strain gages for accurate measurement of mode I stress intensity factor. Mater Des. 2010;31(6):2840–50.

[13] Sarangi H, Murthy KSRK, Chakraborty D. Extent of three parameter zone and optimum strain gage location for eccentric cracked configurations. Appl Mech Mater. 2012;110–116:127–34.

[14] Chakraborty D, Murthy KSRK, Chakraborty D. A new single strain gage technique for the accurate determination of mode I stress intensity factor in orthotropic composite materials. Eng Fract Mech. 2014;124–125:142–54. doi: 10.1016/j.engfracmech.2014.04.011.

[15] Chakraborty D, Murthy KSRK, Chakraborty D. Experimental determination of mode I stress intensity factor in orthotropic materials using a single strain gage. Eng Fract Mech. 2017;173:130–45. doi: 10.1016/j.engfracmech.2017.01.002.

[16] Chakraborty D, Chakraborty D, Murthy KSRK. A strain gage technique for the determination of mixed mode stress intensity factors of orthotropic materials. Compos Struct. 2017;160:185–94. doi: 10.1016/j.compstruct.2016.10.044.

[17] Kondo T, Kurabe Y, Sasaki T, Kurahashi T, Miyashita Y. Use of strain gages for determining generalized stress intensity factors of sharp V-notched plates under transverse bending. Eng Fract Mech. 2014;124–125:248–61. doi: 10.1016/j.engfracmech.2014.04.033.

[18] Murakami T, Kashiwaya H. Experimental determination technique of stress intensity factor and its application. J Eng Mater Technol. 2017;1(Jan 1989):10–5.
[19] Talha A, Mejni F, Boutarfa R, Benseddiq N. A strain gage technique for measuring the mode II stress intensity factors. Eng Fract Mech. 2024;304(Feb):110166. doi: 10.1016/j.engfracmech.2024.110166.
[20] Mejni F, Talha A. An examination of Techniques based on two strain gages for the determination of mode I stress intensity factor in orthotropic composite materials. Theor Appl Fract Mech. 2024;134:104653.
[21] Paul P, Murthy KSRK, Chakraborty D. Experimental determination of mode I notch stress intensity factors using valid strain gage locations. Theor Appl Fract Mech. 2024;133(PA):104573. doi: 10.1016/j.tafmec.2024.104573.
[22] Li Q, Huang C, Gao Z, Wang K, Xu W, Li H. Strain gauge experimental study on mode I rock fracture characteristics under impact loading. Eng Fract Mech. 2021;253(May):107858. doi: 10.1016/j.engfracmech.2021.107858.
[23] Feng L, Qian X. An adaptive learning approach to determine and update crack sizes from strain relaxation data for welded plate joints. Eng Fract Mech. 2022;259:108165.
[24] Yoon J, Lee J, Kim G, Ryu S, Park J. Deep neural network-based structural health monitoring technique for real-time crack detection and localization using strain gauge sensors. Sci Rep. 2022;12(1):1–11. doi: 10.1038/s41598-022-24269-4.
[25] Shah Mansouri T, Lubarsky G, Finlay D, McLaughlin J. Machine learning-based structural health monitoring technique for crack detection and localisation using bluetooth strain gauge sensor network. J Sens Actuator Netw. 2024;13(6):79.
[26] Cheok EWW, Qian X, Quek ST, Si MBI. A digital twin approach toward unlocking elasto-plastic fatigue crack growth rates under negative load ratios. Eng Fract Mech. 2024;301(April):110034. doi: 10.1016/j.engfracmech.2024.110034.
[27] Zhao Y, Liu Y, Xu Z. Statistical learning prediction of fatigue crack growth via path slicing and re-weighting. Theor Appl Mech Lett. 2023;13(6):100477.
[28] Dally JW, Sanford RJ. Strain-gage methods for measuring the opening-mode stress-intensity factor, KI. Exp Mech. 1987;27(4):381–8.
[29] Aabid A. Optimization of reinforcing patch effects on cracked plates using analytical modeling and Taguchi design. Materials (Basel). 2023;16(12):4348.
[30] Aabid A, Hrairi M, Ali JSM, Abuzaid A. Effect of bonded composite patch on the stress intensity factor for a center-cracked plate. IIUM Eng J. 2019 Dec 2. doi: 10.31436/iiumej.v20i2.912.
[31] Aabid A, Nur M, Bin S, Hrairi M, Baig M. Enhancing repair of cracked plate using fiber-reinforced composite patch: Experimental and simulation analysis. Forces Mech. 2025;18(Nov 2024):100302. doi: 10.1016/j.finmec.2024.100302.
[32] Barsoum RS. On quarter-point three-dimensional finite elements in linear elastic fracture mechanics. Int J Numer Methods Eng. 1974;10:25–37.